Structure and Interactions of the Ubiquitin-Conjugating Enzyme Variant Human Uev1a: Implications for Enzymatic Synthesis of Polyubiquitin Chains[†,||]

D. Duong Hau,[‡] Michael J. Lewis,[‡] Linda F. Saltibus,[‡] Landon Pastushok,[§] Wei Xiao,[§] and Leo Spyracopoulos*[,‡]

Department of Biochemistry, University of Alberta, Edmonton, Alberta T6G 2H7, Canada, and Department of Microbiology and Immunology, University of Saskatchewan, Saskatoon, Saskatchewan S7N 5E5, Canada

Received March 30, 2006; Revised Manuscript Received June 19, 2006

ABSTRACT: Lys^{63}-linked polyubiquitination of TRAF2 or TRAF6 is an essential step within the signal transduction cascade responsible for activation of p38, c-Jun N-terminal kinase, and the transcription factor NF-κB. Attachment of ubiquitin (Ub) to a TRAF, and conjugation of Ub molecules to form a polyUb chain, is catalyzed by a heterodimer composed of a catalytically active E2 (hUbc13), involved in covalent bond transfer, and hUev1a, an E2-like protein involved in substrate Ub binding. Given the key biochemical processes in which hUev1a is involved, it is important to determine the molecular basis of the catalytic mechanism for Lys^{63}-linked protein ubiquitination. Nuclear magnetic resonance (NMR) spectroscopy was used to determine the structure of hUev1a and its interactions with Ub and hUbc13. A structural model for the Ub-hUev1a-hUbc13∼Ub tetramer was developed to gain chemical insight into the synthesis of Lys^{63}-linked Ub chains. We propose that a network of hydrogen bonds involving hUbc13-Asp^{81} and Ub-Glu^{64} positions Ub-Lys^{63} proximal to the active site. Interestingly, restrained molecular dynamics simulations in implicit solvent indicate that deprotonation of Ub-Lys^{63} does not involve a general Asp or Glu base and may occur when the amino group approaches the thioester carbonyl carbon near the Bürgi−Dunitz trajectory.

Modification of proteins by covalent attachment of a single or chain of ubiquitin (Ub)[1] molecules is an integral biochemical pathway by which eukaryotes regulate a variety of essential cell processes such as cell cycle progression, oncogenesis, endocytosis, and antigen presentation (*1*−*3*). The first step in the ubiquitination process involves the ATP-dependent covalent attachment of the C-terminus of Ub to an active site cysteine on a Ub-activating enzyme (E1). Subsequently, the activated Ub is transferred to a Ub-conjugating enzyme (E2 or Ubc), also entailing a thioester linkage between the C-terminus of Ub and the E2 active site cysteine. In the final step, a Ub ligase (E3) catalyzes the transfer of Ub from the E2 to the target protein, through formation of an isopeptide bond between the C-terminus of Ub and the side chain amino group of a lysine on the target protein. For certain biochemical processes, Ub molecules are sequentially attached through the C-terminus to the side chain amino group of a lysine on an adjacent Ub to produce a polyUb chain.

In the most studied protein ubiquitination pathway, polyUb chains are linked through the side chain amino group of Lys^{48}, and this process ultimately directs the target protein to the proteasome for degradation (*4*−*6*). In contrast, several types of polyUb chains exist which employ alternative lysine residues in the isopeptide linkage (*3*, *7*, *8*). The specific Ub lysine residue involved in the isopeptide bond is thought to affect the topology of the polyUb chain, consequently determining which proteins bind to the chain and therefore the cellular process in which the target protein is involved (*9*−*11*).

PolyUb chains linked through Lys^{63} have been found to participate in DNA repair (*12*, *13*), the NF-κB signaling pathway (*14*−*17*), activation of stress-activated protein kinases (SAPKs) (*18*), and ribosome function (*19*). The synthesis of Lys^{63} polyUb chains requires an E2 enzyme heterodimer composed of a catalytically active E2 (hUbc13) and an inactive Ubc variant (UEV). hMms2, the UEV involved in DNA repair (*12*, *20*, *21*), differs from hUev1a in that it lacks an N-terminal extension (*20*). Despite having similar sequences, the two UEVs are involved in different cellular processes (*20*); hUev1a is the requisite UEV for interleukin-1 (IL-1) (*22*) and TNFα-induced (*18*) activation of NF-κB and SAPKs and is essential for Bcl10-induced NF-κB activation (*23*).

The mechanism of synthesis of Lys^{63}-linked polyUb chains catalyzed by the hMms2-hUbc13 heterodimer has been

[†] This work was supported by the Canadian Institutes of Health Research (CIHR) and the Alberta Heritage Foundation for Medical Research (AHFMR). L.S. is an AHFMR Medical Research Scholar.

[||] Coordinates have been deposited in the RCSB protein data bank as entry 2HLW. NMR restraints have been deposited in the BMRB data repository under accession number 7219.

* To whom correspondence should be addressed. E-mail: leo.spyracopoulos@ualberta.ca. Phone: (780) 492-2417. Fax: (780) 492-0886.

[‡] University of Alberta.

[§] University of Saskatchewan.

[1] Abbreviations: DSS, 2,2-dimethyl-2-silapentane-5-sulfonic acid; DTT, dithiothreitol; E1, ubiquitin-activating enzyme; E2, ubiquitin-conjugating enzyme; E3, ubiquitin ligase; GST, glutathione *S*-transferase; HSQC, heteronuclear single-quantum coherence; IPTG, isopropyl β-D-thiogalactopyranoside; NF-κB, nuclear factor κB; NMR, nuclear magnetic resonance; NOE, nuclear Overhauser effect; RING, really interesting new gene; S^2, main chain order parameter; SAPKs, stress-activated protein kinases; TRAF, TNFR-associated factor; Ub, ubiquitin; Ubc, ubiquitin-conjugating enzyme; UEV, ubiquitin-conjugating enzyme variant.

10.1021/bi060631r CCC: $33.50
Published on Web 07/27/2006

extensively studied. The structures of free hMms2 and the hMms2-hUbc13 heterodimer have been determined by X-ray crystallography (*24*). A structural model for the synthesis of Lys^{63}-linked diubiquitin chains catalyzed by the hMms2-hUbc13 heterodimer has been produced on the basis of NMR-based chemical shift mapping (*25*). We have recently determined the structure of hMms2 bound to Ub using solution state NMR spectroscopy (*26*). Furthermore, the entropic contribution to the binding free energy due to changes in main chain and side chain dynamics for the Ub-hMms2 interaction have been estimated using NMR spectroscopy (*27*). These studies are important for laying the foundation for a detailed understanding of the mechanism by which hMms2-hUbc13 catalyzes the synthesis of Lys^{63}-linked polyUb chains. In contrast to hMms2, there are fewer detailed atomic resolution studies regarding the structure and function of hUev1a (*28*). A recent study has determined the structure of the hUev1a-hUbc13 heterodimer in complex with the E3 ligase CHIP, and the heterodimer resembles the structure of hMms2-hUbc13 (*29*). However, for this structure, there are no details regarding the interaction of hUev1a-hUbc13 with either donor or acceptor Ub or the N-terminal tail of hUev1a. In addition, the biological relevance is not clear, given that the hUev1a-hUbc13 heterodimer has been shown to function in the immune response through interactions with the E3 ligases TRAF2 and TRAF6 (*18*, *22*).

It is important to develop an in-depth understanding of the structure and function of hUev1a and its role in polyUb chain catalysis, considering its exclusive cellular functions compared to other UEVs. In this study, we present the NMR-derived solution structure and main chain dynamics of hUev1a. In addition, NMR chemical shift mapping experiments have been used to identify the binding sites of hUev1a upon interaction with Ub or hUbc13. We have also employed chemical shift mapping experiments to investigate the interaction between hUbc13 within the hUbc13-hMms2 heterodimer and Ub that is primarily noncovalently bound to hMms2. Finally, we have used a classical mechanical approach with restrained molecular dynamics simulations and an implicit solvent model to gain insight into the catalysis of the synthesis of Lys^{63}-linked diubiquitin chains by hUev1a-hUbc13. Analysis of the simulations indicates that for the mechanism of acceptor Ub-Lys^{63} aminolysis of the donor Ub-hUbc13 thioester bond, there are no Asp or Glu residues that can act as a general base to abstract a proton from the ϵ-amino of Ub-Lys^{63}. The simulation also indicates that, depending on the angle of approach of the amino group from donor Ub-Lys^{63} to the carbonyl carbon of the thioester bond, instantaneous large and negative changes in the pK_a of the amino group are observed, such that deprotonation and subsequent nucleophilic attack on the carbonyl carbon become possible.

EXPERIMENTAL PROCEDURES

Cloning and Expression. (A) hUev1a. hUev1a was cloned as a GST fusion protein as previously described (*30*). Expression of hUev1a was conducted as previously described for hMms2 (*27*) with the following exceptions. For production of [U-^{15}N,U-^{13}C]-hUev1a, the M9 minimal media (*31*) contained 2 g/L [U-99% ^{13}C]-D-glucose and 1 g/L [U-98% ^{15}N] ammonium sulfate as the only carbon and nitrogen sources, respectively. For all protein purification buffers containing NaCl, the salt concentration was 250 mM.

The protocol for the production of [U-^{15}N]- or [U-^{15}N,U-10% ^{13}C]-hUev1a was identical to the protocol for [U-^{15}N,U-^{13}C]-hUev1a with the exception that 2 g/L [U-99% ^{13}C]-D-glucose in the minimal media was substituted by 4 g/L [^{12}C]-D-glucose or 0.2 g/L [U-99% ^{13}C]-D-glucose with 1.8 g/L [^{12}C]-D-glucose, respectively. The protocol for unlabeled hUev1a expression was identical to that detailed above with the exception that LB medium, containing 50 μg/mL ampicillin and 25 μg/mL chloramphenicol, was used instead of M9 minimal medium.

(B) hUbc13. Expression and purification of unlabeled and [U-^{15}N,U-^{13}C]-hUbc13K92R was conducted in a fashion similar to that previously described for the protein hMms2 (*26*, *27*). The protocol for unlabeled hUbc13 expression was similar to that for unlabeled hUev1a, as described above.

(C) hMms2. [U-~100% ^{2}H]-hMms2 was expressed as previously described for [U-^{13}C,U-^{15}N,U-~50% ^{2}H]-hMms2 (*27*), with the exception that M9 salts were prepared in 100% D_2O with 2 g of [U-~98% 1,2,3,4,5,6,6-^{2}H]-D-glucose and 0.5 g of unlabeled ammonium sulfate.

(D) Ubiquitin. Expression and purification of [U-^{15}N]-UbK48R was conducted similarly to that previously described for [U-^{15}N,U-^{13}C]-UbK48R (*26*).

NMR Spectroscopy. (A) hUev1a. For all NMR experiments involving hUev1a, full-length protein was employed, and the sequence included five N-terminal vestigial residues (Gly-Pro-Leu-Gly-Ser) from a cloning artifact. All samples contained 9:1 H_2O:D_2O buffer with 50 mM NaH_2PO_4, 250 mM NaCl, 0.9 mM DTT, and 1.7 mM DSS at pH 7.0. For NMR experiments involving [U-^{15}N,U-^{13}C]-hUev1a, the protein concentration was ~1 mM for 300 μL samples in Shigemi microcell NMR tubes. For all other samples, standard 5 mm i.d. NMR tubes were used with protein concentrations of ~0.75 mM for [U-^{15}N,U-10% ^{13}C]-hUev1a and ~0.5 mM for all other experiments.

For hUev1a, all NMR spectra were collected on a Varian Unity INOVA 600 MHz NMR spectrometer with the exception of ^{15}N-separated 3D NOESY HSQC (*32*) and ^{13}C-separated 3D NOESY HSQC spectra, which were recorded on a Varian Unity INOVA 800 MHz NMR spectrometer. All NMR experiments were performed at 30 °C. Spectra were processed and analyzed with the NMRPipe (*33*) and NMRView (*34*) programs, respectively.

(B) hUbc13. All NMR spectra were obtained using a Varian Unity INOVA 600 MHz NMR spectrometer. The NMR sample for assignment of [U-^{15}N,U-^{13}C]-hUbc13 was 300 μL for a SHIGEMI microcell NMR tube and contained 9:1 H_2O:D_2O with 50 mM phosphate (pH 7.5), 250 mM NaCl, 1 mM DTT, 1 mM DSS, and 3 μL of 100× stock protease inhibitor cocktail I (Calbiochem catalog no. 539131) with ~0.5 mM hUbc13.

Chemical Shift Assignment for hUev1a. Sequential resonance assignments were accomplished using a combination of the HNCACB (*35*, *36*), CBCA(CO)NH (*36*, *37*), and HNCA (*39*) experiments. Assignment of $^{1}H_{\alpha}$ and side chain ^{1}H and ^{13}C atoms, excluding those found on aromatic and methionine methyl groups, was accomplished with the (H)CC(CO)NH-TOCSY (*41*), H(CC)(CO)NH-TOCSY (*39*, *40*), HCCH-TOCSY (*41*, *42*), MQ-(H)C$C_m$$H_m$-TOCSY (*43*), HNHA (*44*), and HNHB (*45*) experiments. Aromatic atoms

were assigned using the (HB)CB(CGCD)HD (*46*), (HB)CB(CGCDCE)HE (*46*), (H)CCH-TROSY (*47*, *48*), aromatic 2D $^{1}H-^{13}C$ HSQC (*50*), ^{15}N-separated 3D NOESY HSQC (*32*), and ^{13}C-separated 3D NOESY HSQC experiments, in conjunction with structures determined late in the refinement process. Resonances for methionine methyl groups were determined using the 2D $^{1}H-^{13}C$ HSQC, ^{15}N-separated 3D NOESY HSQC, and ^{13}C-separated 3D NOESY HSQC experiments, with analyses of structures during the refinement process. A nonconstant time 2D $^{1}H-^{13}C$ HSQC experiment using [U-^{15}N,U-10% ^{13}C]-hUev1a was used to stereospecifically assign the side chain methyl groups of valine and leucine residues (*50*).

Chemical Shift Assignment for hUbc13. The main chain atoms of [U-^{15}N,U-^{13}C]-hUbc13 were unambiguously assigned using a combination of the HNCACB and CBCA(CO)NNH experiments. Side chain atoms were assigned using the (H)CCTOCSY(CO)NNH and H(CC)TOCSY(CO)NNH experiments and the HCCH-TOCSY experiment. All spectra were processed using the program NMRPipe, and chemical shift assignment was accomplished using the program Sparky (*51*).

Structure Calculations for hUev1a. Interproton distance restraints were obtained from the ^{15}N-separated 3D NOESY HSQC (*32*) and ^{13}C-separated 3D NOESY HSQC experiments. A total of 2080 distance restraints were obtained from NOE resonance peak intensities and were calibrated within the range of 1.7−6.0 Å as previously described (*52*). Due to resonance peak overlap, 20 restraints were lengthened by an additional 0.07−1.37 Å.

$^{3}J_{HNH\alpha}$ coupling constants obtained from the HNHA experiment were used to calculate restraints for the main chain ϕ dihedral angle (*44*). The error assigned to each coupling constant was 1 Hz. Additional ϕ and ψ dihedral restraints were generated by the TALOS program using $^{1}H_{\alpha}$, $^{13}C_{\alpha}$, $^{13}C_{\beta}$, and main chain ^{15}N chemical shifts (*53*). The error of each predicted restraint was set to twice the standard deviation of the predicted angle. For residues that the TALOS program was unable to predict a ψ dihedral restraint, restraints were produced using the $d_{N\alpha}/d_{\alpha N}$ intensity ratio obtained from the ^{15}N-separated 3D-NOESY HSQC experiment, and the error was set to ±100° (*54*). Main chain dihedral restraints were imposed only if the residue did not show a resonance peak in a 2D $^{1}H-^{15}N$ CLEANEX-PM FHSQC NMR spectrum with a 100 ms mixing time (*55*) and the dihedral restraint was within the range of angles observed in structures determined only with NOE distance restraints.

In addition to distance and dihedral angle restraints, main chain hydrogen bond restraints were included for α-helical or β-strand regions as follows: hydrogen bonds were predicted from working structures using the program VADAR (*56*), and $O-H_N$ distance restraints were set to 2.05 ± 0.25 Å. In addition, hydrogen bond restraints were imposed only if a residue did not display a resonance peak in a 100 ms mixing time 2D $^{1}H-^{15}N$ CLEANEX-PM FHSQC NMR spectrum.

Following structure refinement, two hundred structures were calculated using the torsion angle-based simulated annealing protocol in CNS 1.1 (*57*), starting from an extended conformation for hUev1a that lacked the vestigial residues from the cloning artifact. Structural statistics were calculated using the programs AQUA and PROCHECK-NMR (*58*), in-house written scripts, PyMOL (*59*), and MOLMOL (*60*). Molecular structure graphics were produced with the program PyMOL.

^{15}N NMR Relaxation Studies for hUev1a. ^{15}N-T_1, ^{15}N-T_2, and $\{^{1}H\}^{15}N$ NOE data were collected, processed, and analyzed as previously described (*27*). NMR spectra were acquired at 30 °C and two magnetic field strengths (600 and 500 MHz). For the T_1 data, spectra were acquired with the following relaxation delays: 10, 50, 120, 200, 300, 400, 500, 700, and 800 ms; the same delays were used for the T_1 data collected at 600 MHz, with the exception that an additional spectrum with a relaxation delay of 1 s was collected. Delays of 10, 30, 50, 70, 90, 110, 130, and 150 ms were used for the measurement of T_2 at 500 and 600 MHz. The delays between transients were 1.2 and 3.0 s for the T_1 and T_2 pulse sequences, respectively, at both magnetic field strengths. $\{^{1}H\}^{15}N$ NOEs were measured as previously described (*27*). An analysis of rotational diffusion anisotropy and a Lipari−Szabo model-free analysis were conducted using the program Mathematica (*61*), using an approach similar to that recently described (*27*).

Titration of hUbc13 into [U-^{15}N]-hUev1a. hUbc13 was titrated into a 300 μL sample of ∼0.5 mM [U-^{15}N]-hUev1a in a Shigemi microcell NMR tube in the following manner. A 2D $^{1}H-^{15}N$ HSQC spectrum of [U-^{15}N]-hUev1a was collected in the absence of hUbc13. Subsequently, 0.4 mL of ∼1.5 mM hUbc13 was added to the sample and concentrated to 300 μL with a 10000 NMWL centrifugal filter device to give a hUbc13:hUev1a ratio of approximately 2:1, and a 2D $^{1}H-^{15}N$ HSQC NMR spectrum of the sample was acquired. An additional 0.2 mL of ∼1.5 mM hUbc13 was added to the sample and concentrated to produce an NMR sample containing 3:1 hUbc13:hUev1a, and a 2D $^{1}H-^{15}N$ HSQC NMR spectrum was collected. Main chain amide $^{1}H-^{15}N$ resonance peaks in the 2D $^{1}H-^{15}N$ HSQC NMR spectra for each of the titration points were assigned on the basis of proximity to resonance peaks in the 2D $^{1}H-^{15}N$ HSQC NMR spectrum for free hUev1a. Chemical shift changes for the main chain amide $^{1}H-^{15}N$ resonance peaks were calculated as previously described (*25*). Chemical shift changes greater than the average chemical shift change plus one standard deviation ($\Delta\delta_{avg} + 1\sigma$) were considered strongly significant, and chemical shift changes between $\Delta\delta_{avg}$ and ($\Delta\delta_{avg} + 1\sigma$) were considered moderately significant.

Chemical Shift Mapping of [U-^{15}N]-hUev1a upon Titration with Ub. Chemical shift mapping of [U-^{15}N]-hUev1a upon titration with Ub was accomplished using previously published titration data (*28*) and main chain amide $^{1}H-^{15}N$ chemical shift assignments for hUev1a determined herein.

Chemical Shift Mapping of [U-^{15}N,U-^{13}C]-hUbc13-[U-∼100% ^{2}H]-hMms2 upon Titration with [U-^{15}N]-Ub. [U-^{15}N,U-^{13}C]-hUbc13 was mixed with two separate 4.8 mL aliquots of 0.01 mM [U-∼100% ^{2}H]-hMms2 and was concentrated to 350 μL for each aliquot with a 10000 NMWL centrifugal membrane filtration device and placed into a Shigemi microcell NMR tube. The final concentration for hUbc13-hMms2 was ∼0.3 mM. The buffer was similar to that for free [U-^{15}N,U-^{13}C]-hUbc13 (see section entitled NMR Spectroscopy). For the two aliquots of [U-∼100% ^{2}H]-hMms2, saturation of hUbc13 with hMms2 was monitored by observing the disappearance of the resonance peak for

the methyl group resonance of free hUbc13 Met[72] and the simultaneous appearance of the bound peak in 2D $^{1}H-^{13}C$ HSQC NMR spectra (data not shown). Three additions of ~1 mg of solid [U-^{15}N]-Ub were added directly to the [U-^{15}N,U-^{13}C]-hUbc13-[U-~100% ^{2}H]-hMms2 complex to yield molar ratios of ~1:1, ~2:1, ~3:1, and ~4:1 Ub:hUbc13-hMms2. A 2D $^{1}H-^{15}N$ HSQC spectrum of [U-^{15}N,U-^{13}C]-hUbc13 was collected for each addition of solid Ub. Main chain amide $^{1}H-^{15}N$ resonance peaks in the 2D $^{1}H-^{15}N$ HSQC NMR spectra for each of the titration points were assigned on the basis of proximity to resonance peaks in the 2D $^{1}H-^{15}N$ HSQC NMR spectrum for free hUbc13. Several cross-peaks whose chemical shifts changed significantly upon addition of [U-~100% ^{2}H]-hMms2 could not be assigned. However, these unassigned peaks were not observed to shift upon titration with Ub. For the final titration point, chemical shift changes for the main chain amide $^{1}H-^{15}N$ resonance peaks of [U-^{15}N,U-^{13}C]-hUbc13 upon titration with Ub were calculated as described for hUev1a.

Given that [U-^{15}N]-Ub was titrated into [U-^{15}N,U-^{13}C]-hUbc13-[U-~100% ^{2}H]-hMms2, in addition to following chemical shift changes for hUbc13, those for the main chain amide $^{1}H-^{15}N$ resonance peaks of [U-^{15}N]-Ub were also calculated using chemical shifts from the first titration point with Ub (1:1 Ub:hUbc13-hMms2) and the chemical shifts of free Ub (*26*).

Model Building for the hUev1a-(Ub-Gly[76]~Cys[87]-hUbc13)-Ub Tetramer. To gain insight into the mechanism of catalysis of synthesis of polyUb chains by hUbc13-UEV heterodimers, a model for the Ub-hUev1a-hUbc13 trimer was built using the programs PyMOL (*59*) and HADDOCK (*62*) as previously described (*26*) by superimposing the structure of hUev1a minus the 35 flexible N-terminal residues onto the structure of hMms2 in the hMms2-hUbc13 heterodimer and assuming that intermolecular NOE restraints between acceptor Ub and hUev1a are the same as those observed for hMms2 (*26*). This model was then used to construct the Ub-hUev1a-hUbc13~Ub tetramer. For the thioester bond between the C-terminus of donor Ub (···Gly[75]-Gly[76]-COO-) and the side chain of the active site Cys[87] from hUbc13, bond lengths and angles were estimated from the structure of *S*-methyl thioacetate, geometry optimized with the program Gaussian 03 (*63*) at the B3LYP/6-31G** level with stationary point verification using a frequency calculation (*64*). Fixed partial charges for the main chain and side chain atoms of Ub-Gly[76] and hUbc13-Cys[87] within a thioester-linked Cys-Gly model compound with capped N- and C-termini were determined using two-stage RESP fits (*65*, *66*) using the program Gaussian 03 (B3LYP/6-31G**//B3LYP/6-31G* level of theory) and the AMBER 8 biomolecular simulation suite of programs (*67*, *68*).

Following initial model building, the Ub-hUev1a-hUbc13~Ub tetramer was subjected to energy minimization with the inclusion of a distance restraint between the ϵ-amino group of Ub-Lys[63] and the carbonyl carbon of the thioester bond using the AMBER package. To allow for conformational averaging for the initial Ub-hUev1a-hUbc13~Ub model, a 200 ps restrained molecular dynamics simulation was conducted at 300 K using the AMBER suite of programs. Given that an unrestrained, nanosecond time scale molecular dynamics simulation is not practical in the present case, harmonic restraints were employed for all atoms except those from donor Ub thioester-linked to hUbc13, the loop (residues 61−66) containing residues Glu[64] and Lys[63] from acceptor Ub, active site residues from hUbc13 (residues 79−94), and the loop between hUbc13 α-helices 2 and 3 (residues 115−122). Moreover, a distance restraint between the amino nitrogen from Lys[63] of the donor Ub and the carbonyl carbon of the thioester bond was included. The restraint had a flat bottom from 2 to 3 Å, was parabolic from 3.0 to 4.0 Å, and linear beyond, with a force constant of 32 kcal/(mol·Å^2). Additional details for the simulation include the use of the ff99 force field (*69*), a time step of 2 fs, covalent bonds to hydrogen were restrained using SHAKE (*70*), temperature was maintained using a Berendsen temperature bath (*71*), the cutoff for nonbonded interactions and generalized Born radii was 16 Å, salt concentration was 100 mM, and the initial generalized Born model developed by Case and coworkers was used (*72*). ΔpK_a values were calculated for Ub-Lys[63], Ub-Glu[64], and hUbc13-Asp[81] using the coordinates of structures from every 0.1 ps step in the molecular dynamics simulation, the thermodynamic cycle in Figure 1, and eqs 1−3 from ref *73*. For the pK_a calculations, all residues except the residue of interest (one of Ub-Lys[63], Ub-Glu[64], or hUbc13-Asp[81]) were assumed to be in the protonation states expected for pH 7.0.

To check accuracy, ΔpK_a values were also calculated as described above for the semiburied Asp[70]−His[31] salt bridge in T4 lysozyme (3LZM), the Asp[83]−Arg[136] salt bridge in xylanase (1XNB), the partly buried Asp[81]−Arg[85] salt bridge, and the surface-exposed residues Lys[94] and Asp[118] in the hUbc13-hMms2 heterodimer (1J7D) and Asp[26] in thioredoxin that is partly buried in a hydrophobic environment (1TRX). For the surface-exposed side chains in hUbc13-hMms2, pK_a values are within ~±0.5 pH unit of the common values. While the magnitudes of ΔpK_a values for Asp residues involved in buried salt bridges are not accurately reproduced, the signs of the shifts match experimental values for xylanase and T4 lysozyme. Similarly for Asp[26] of thioredoxin, the pK_a upshift is correctly predicted, but the magnitude is not accurate. Thus, the sign of the pK_a shifts determined in the calculations can be used to assess whether a particular ionizable side chain can potentially act as a general acid or base.

RESULTS

Solution State NMR Structure of hUev1a. Of the total ^{1}H, ^{13}C, and ^{15}N hUev1a chemical shift resonances, 87% were assigned. Most of the valine and leucine methyl groups were stereospecifically assigned with the exception of Val[130], Leu[10], and Leu[16] (due to chemical shift overlap). Of the 200 structures that were calculated, the 15 lowest energy structures were selected for the ensemble (Figure 1A). The solution state structure of hUev1a indicates that the N-terminal region of the protein (35 residues) is unstructured, whereas the bulk of the remaining residues form a core domain with a typical UEV fold. The N-terminal region of the structure shows an average main chain rmsd value of 9 ± 3 Å upon superposition to the average structure. The lack of structure for the N-terminus is supported by three observations. First, residues within the N-terminal region are deficient in NOE restraints, despite the fact that 86% of the atoms within this region have been assigned. These residues have an average of 3 NOEs per residue compared to the

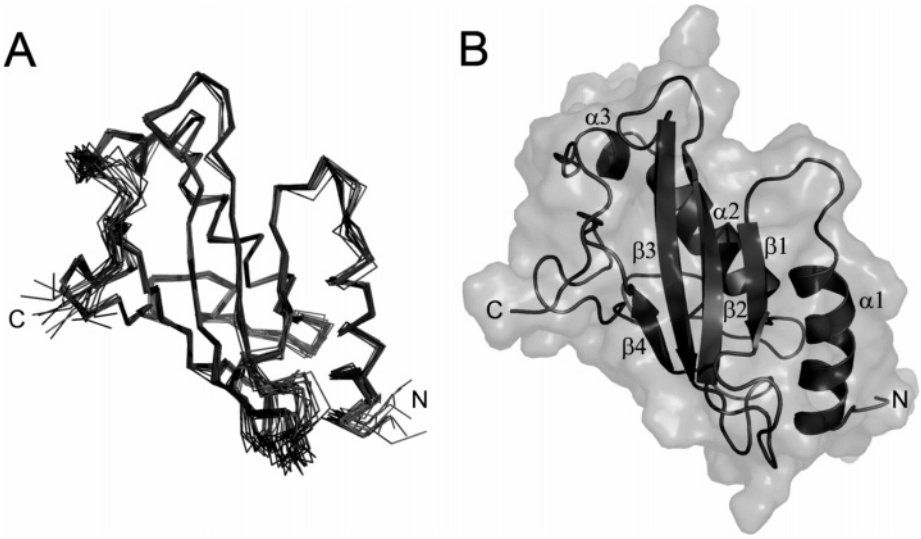

FIGURE 1: Solution structure for the core domain of hUev1a. (A) Backbone superposition of the 15 structures for the core of hUev1a (residues 33−170). (B) Ribbon representation of the minimized average structure of hUev1a (residues 33−170), depicting secondary structural elements.

structured UEV core region that has an average of 15 NOEs per residue. Second, nearly all of the 35 N-terminal residues give rise to a resonance peak in a 100 ms mixing time 2D $^{1}H-^{15}N$ CLEANEX-PM FHSQC experiment, indicating that the main chain amide protons for these residues are in fast exchange with water. Thus, these residues are likely to be solvent accessible and presumably unstructured. Finally, the main chain amide ^{1}H chemical shifts from these residues are found within a narrow region from 7.8 to 8.5 ppm, consistent with a lack of secondary structure.

The core structured region displays a typical UEV fold composed of an N-terminal α helix, α1 (36−49), which is followed by a four-strand, antiparallel β sheet (β1, 56−59; β2, 69−77; β3, 86−94; and β4, 104−107) and two C-terminal α helices (α2, 140−152; and α3, 154−157), with α2 forming extensive contacts with one face of the β sheet (Figure 1B). For the ensemble of 15 structures, the main chain atoms within the structured region have an rmsd value of 0.98 ± 0.15 Å, whereas regions of secondary structure have a main chain rmsd value of 0.43 ± 0.07 Å. Structural statistics are summarized in Table 1.

Main Chain Dynamics: ^{15}N-T_1, ^{15}N-T_2, and NOE Data. Main chain amide ^{15}N NMR relaxation data were obtained at 500 MHz and [600] MHz for 118 [118] of a total of 170 residues. Uncharacterized residues were either prolines, in rapid exchange with water or partially/completely overlapped in the 2D $^{1}H-^{15}N$ HSQC NMR spectra. The average T_1 for all residues is 562 ± 61 [721 ± 98] ms, with an average error of 26 [24] ms. The average T_2 for all residues is 97 ± 45 [90 ± 41] ms, with an average error of 3 [5] ms. The average NOE for all residues is 0.65 ± 0.24 [0.75 ± 0.17], with an average error of 0.08 [0.05]. The theoretical values for T_1, T_2, and NOE are 652 [844] ms, 88 [83] ms, and 0.74 [0.75], respectively, and correspond closely to the experimental averages. The theoretical values were determined using τ_m, τ_f, and S^2 values of 9.84 ns, 25 ps, and 0.85, respectively.

S^2 values were calculated for main chain amide groups from data obtained at 500 and 600 MHz (Figure 2A). The average S^2 value is 0.8 ± 0.1. Loop 1 (L1) and the extreme C-terminal residue display low S^2 values. Due to peak overlap or poor signal to noise ratio, many S^2 values were not calculated for the N-terminal region (residues 1−35).

Table 1: Characteristics of the Ensemble of Structures for hUev1a

distance restraints	
total	2080
intraresidue	843
medium ($1 \leq \|i-j\| \leq 4$)	659
long ($\|i-j\| \geq 5$)	578
hydrogen bonds	36
dihedral restraints	
$^{3}J_{HNHA}$-derived ϕ	56
TALOS-derived ϕ	69
TALOS-derived ψ	68
$d_{N\alpha}/d_{\alpha N}$-derived ψ	4
restraint violations[a]	
distance restraints (>0.3 Å) (%)	0
distance restraints (≥0.1 Å, ≤0.3 Å) (%)	0.2
distance restraints (<0.1 Å) (%)	5.7
dihedral restraints (>0°) (%)	6.5
maximum dihedral violation (deg)	2.6
Ramachandran plot	
allowed region (%)	97.6
generously allowed region (%)	1.9
disallowed region (%)	0.5
rmsd (Å)	
heavy atoms[b]	1.6 ± 0.1
backbone atoms[b]	1.0 ± 0.2
secondary structure backbone atoms[c]	0.43 ± 0.07
rmsd from ideal covalent geometry	
bonds (Å)	0.00147 ± 0.00005
angles (deg)	0.329 ± 0.003
impropers (deg)	0.193 ± 0.007

[a] All 15 structures in the final ensemble were included in the calculations. [b] Calculated for residues 36−170. [c] Calculated for residues 36−49, 56−59, 69−77, 86−94, 104−107, 140−152, and 154−157.

Chemical Shift Mapping of [U-^{15}N]-hUev1a upon Titration with hUbc13. From a total of 134 assignments for free Uev1a, 104 resonance peaks were assigned in the hUbc13-bound state. Unassigned residues included those whose resonance peaks vanished upon binding of hUbc13 or those that could not be unambiguously assigned. Two discrete peaks were observed for some of the resonances in the spectrum containing 2:1 hUbc13:hUev1a, indicating that the binding

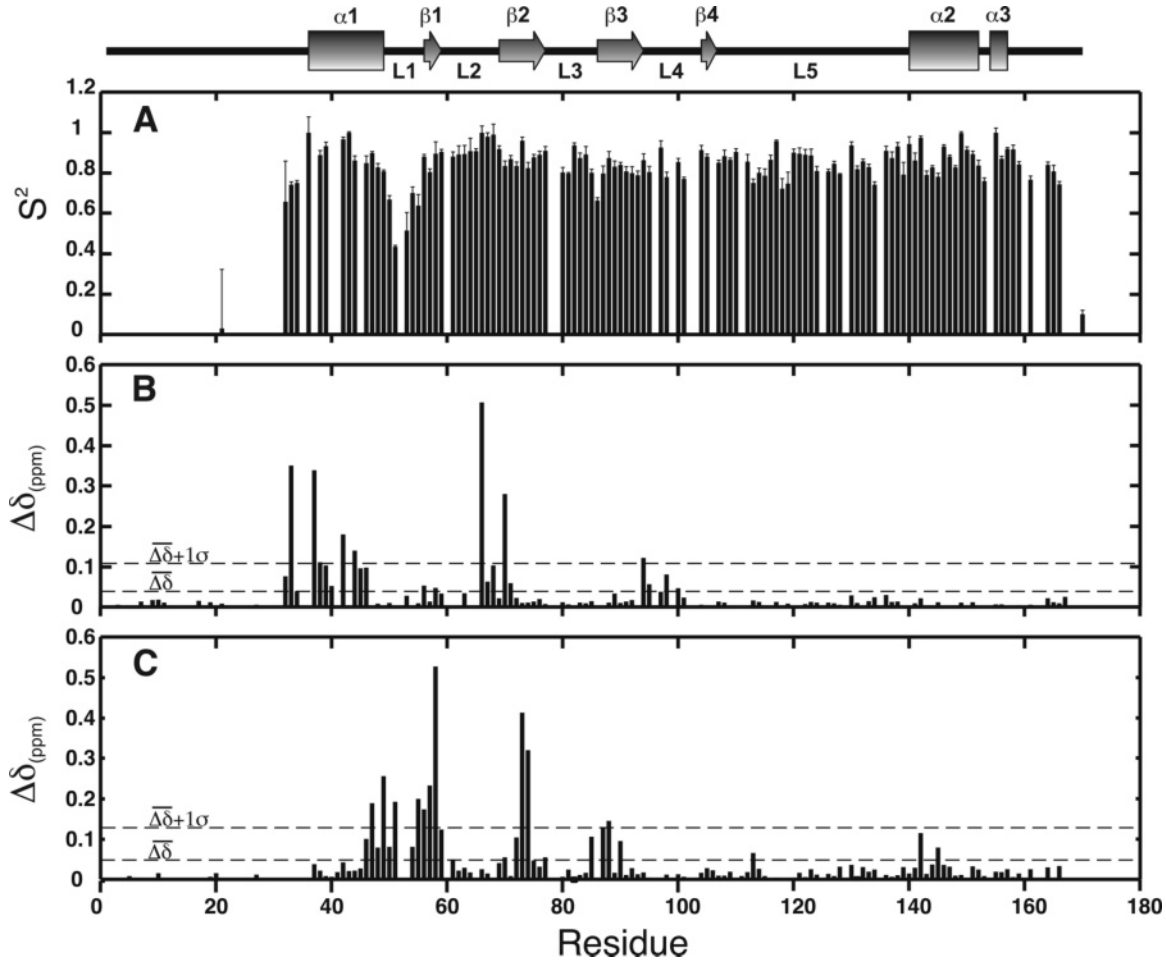

FIGURE 2: Main chain dynamics and protein−protein interactions for hUev1a. (A) Plot of main chain amide S^2 values for free hUev1a, calculated from data collected at 500 and 600 MHz. Comparison of main chain amide ^1H and ^{15}N chemical shifts for hUev1a upon binding hUbc13 (B) and Ub (C).

event occurs in slow exchange on the NMR time scale and that hUev1a is not completely saturated with hUbc13. hUev1a may not be fully bound to hUbc13 at a 2:1 hUbc13:hUev1a ratio due to either an underestimation of hUbc13 concentration or homodimerization of hUbc13. The average change in chemical shift for the 104 resonance peaks is 0.04 ± 0.07 ppm. hUev1a $^1H-^{15}N$ main chain amide resonances observed to undergo significant and moderate chemical shift changes upon addition of hUbc13 are shown in Figure 2B and involve residues clustered around the α1 helix and the neighboring loop or strand regions (Figure 3C).

Chemical Shift Mapping of [U-^{15}N]-hUev1a upon Titration with Ub. Main chain amide $^1H-^{15}N$ chemical shift changes for hUev1a upon titration with Ub are shown in Figure 2C. The average change in chemical shift is 0.05 ± 0.08 ppm for the 112 assigned resonance peaks. Residues whose chemical shift changes were found to be significantly and moderately affected upon titration with Ub are shown in Figure 2C and localized to a surface of hUev1a that is comprised of the C-terminal end of helix α1, loop 1, and portions of the β1, β2, and β3 strands (Figure 3A).

Chemical Shift Mapping of [U-^{15}N,U-^{13}C]-hUbc13-[U-∼100% ^{2}H]-hMms2 upon Titration with [U-^{15}N]-Ub. Main chain amide $^1H-^{15}N$ chemical shift changes for hUbc13 in 1:1 [U-^{15}N,U-^{13}C]-hUbc13-[U-∼100% ^{2}H]-hMms2 upon addition of a 4-fold molar excess of [U-^{15}N]-Ub are shown in Figure 4A. From a total of 124 assignments for free Ubc13, 34 resonance peaks were assigned in the hMms2-bound state. Unassigned residues included those whose resonance peaks disappeared upon binding of hMms2, those that could not be unambiguously assigned, in rapid exchange with water, or overlapped. The average chemical shift change is 0.07 ± 0.03 ppm.

$^1H-^{15}N$ chemical shift changes for Ub binding to 1:1 [U-^{15}N,U-^{13}C]-hUbc13-[U-∼100% ^{2}H]-hMms2 are shown in Figure 4B. From a total of 73 assignments for free Ub, 59 resonance peaks were assigned in the complex with 1:1 [U-^{15}N,U-^{13}C]-hUbc13-[U-∼100% ^{2}H]-hMms2. Unassigned residues included those that could not be assigned, were overlapped, or were in rapid exchange with water. The average chemical shift change is 0.01 ± 0.01 ppm.

DISCUSSION

Despite sharing high sequence homology, the ubiquitin-conjugating enzyme variants hMms2 and hUev1a are involved in distinct cellular processes, and it is not clear how their sequence divergence translates into functional differences between these proteins (*20*). In this study, our objectives were to gain a more detailed understanding of the mechanism underlying hMms2 and hUev1a catalyzed Lys^{63}-linked polyUb chain formation and the impact of sequence differences between hMms2 and hUev1a by determining the

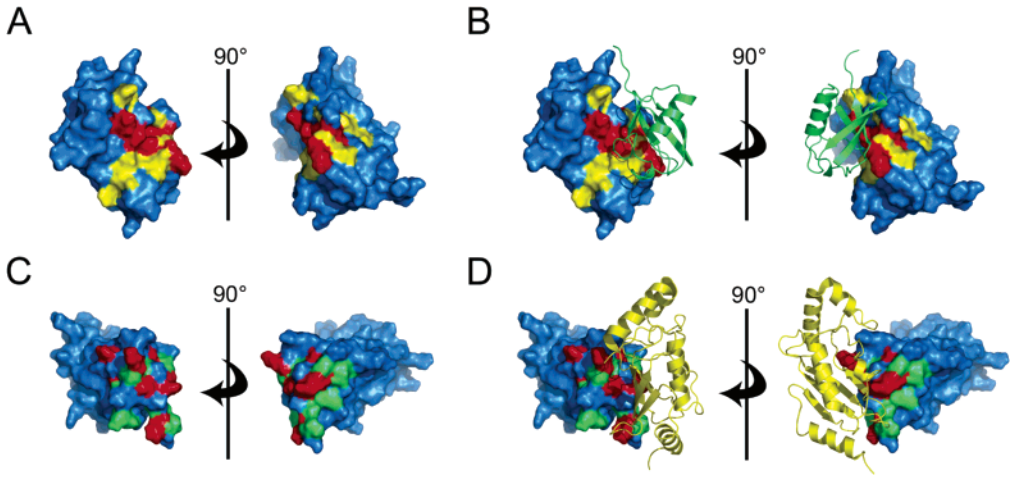

FIGURE 3: Chemical shift maps for hUev1a upon binding of Ub and hUbc13. Surface representation of free hUev1a (A, C), hUev1a superimposed onto hMms2 in the hMms2-Ub structure (B), or hUev1a superimposed hMms2 in the hMms2-hUbc13 structure (D). hUev1a residues significantly ($\Delta\delta > \Delta\delta_{avg} + 1\sigma$) and moderately ($\Delta\delta_{avg} + 1\sigma > \Delta\delta > \Delta\delta_{avg}$) affected upon titration with Ub (green) are colored in red and yellow, respectively (A, B). hUev1a residues strongly ($\Delta\delta > \Delta\delta_{avg} + 1\sigma$) and moderately ($\Delta\delta_{avg} + 1\sigma > \Delta\delta > \Delta\delta_{avg}$) affected upon titration with hUbc13 (yellow) are colored in red and green, respectively (C, D).

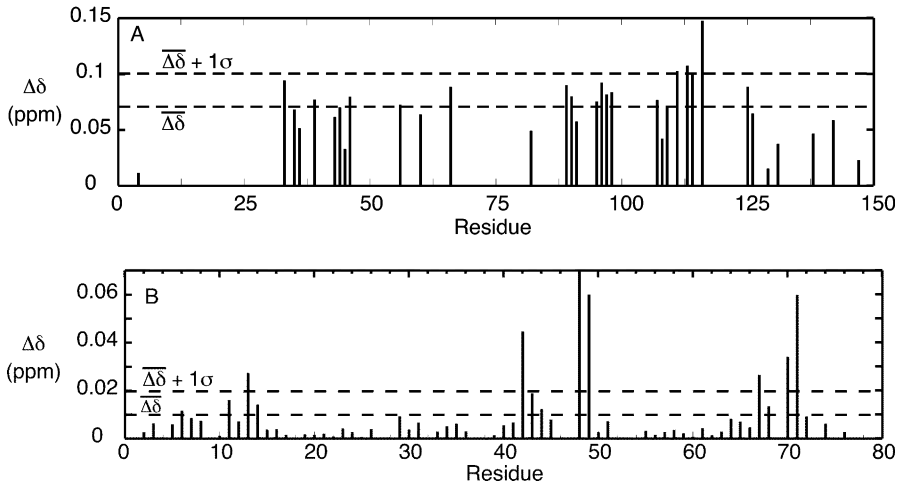

FIGURE 4: Chemical shift maps for Ub and hUbc13 upon binding of Ub to the hUbc13-hMms2 heterodimer. (A) Chemical shift changes for hUbc13 upon titration with Ub. (B) Chemical shift changes for Ub upon titration of Ub into hUbc13-hMms2. Significant chemical shift changes are defined as in the legend to Figure 3.

structure, main chain dynamics, and protein interactions for hUev1a. In addition, the interaction between Ub and hUbc13 in the ternary Ub-hUbc13-hMms2 noncovalent complex was investigated using chemical shift mapping. The results have allowed for a structural comparison between hMms2 and hUev1a and the development of a model for catalysis of the synthesis of Lys^{63}-linked diubiquitin chains.

Structural Comparison to hMms2. hMms2 is ~90% identical in sequence to residues 26−170 of hUev1a. Therefore, it is expected that the structured core region of hUev1a should adopt a tertiary structure similar to that of hMms2. Alignment of the main chain atoms of residues 35−170 of the minimized average structure of hUev1a with residues 10−145 of hMms2 (PDB ID 1J74) (*24*) gives an rmsd value of 1.3 Å, indicating that the two structures are similar. The functional differences between hMms2 and hUev1a may be a consequence of the presence of the N-terminal tail of hUev1a that is not present in hMms2 or the 10 residues that differ between the core domains of the two proteins. The results presented herein indicate that the N-terminal tail is not involved in interactions with hUbc13 or Ub and, therefore, may be involved in interactions between the hUev1a-hUbc13 heterodimer and its cognate E3 Ub ligase (vide infra).

Dynamics of hUev1a. The flexibility of a protein main chain can be assessed through NMR-based measurement of order parameters, or S^2 values, for main chain $^1H-^{15}N$ pairs (*27*). S^2 values represent the amplitude of spatial restriction for a main chain $^1H-^{15}N$ bond vector. Characterization of the S^2 values of free hUev1a allows for assessment of regions of flexibility within a protein and detection of specific changes in protein flexibility, or entropy, upon interaction with ligands (*74*, *75*).

The S^2 values for main chain amide groups of hUev1a (Figure 2A) are similar to those of free hMms2 (*27*). For both hMms2 and hUev1a, the majority of residues have S^2 values around 0.82, while residues found in L1 and at the C-terminus display smaller S^2 values, indicating that the C-terminus and L1 are flexible. Given the empirical correlation between protein structure and main chain amide S^2 values (*76*), the similarity between S^2 values for hMms2 and

hUev1a is consistent with the similarity of their tertiary structures.

The majority of S^2 values for hUev1a (~0.82) are typical for regions of canonical secondary structure in proteins, including regions involved in the binding of hUbc13 and Ub. Therefore, a large unfavorable decrease in entropy for the main chain of hUev1a is not expected upon binding either hUbc13 or Ub. For example, we have estimated the entropy change for the main chain of hMms2 (~150 residues) upon Ub binding to be ~33 kJ mol^{-1} ($-T\Delta S$) (*27*). In comparison, the per residue conformational entropy change for the protein main chain upon folding has been estimated to be around 3 kJ mol^{-1} residue^{-1} (*77*).

Interaction with hUbc13. The main chain amide $^1H-^{15}N$ chemical shift changes for hUev1a upon interaction with hUbc13 indicate that the binding interface is composed of residues from the N-terminus, helix α1, and L2 of hUev1a (Figure 3C). An alignment of the structure of hUev1a with the structure of hMms2 bound to hUbc13 (PDB ID 1J7D) shows that the NMR chemical shift-based binding interface includes hUev1a residues that are adjacent to, or within the vicinity of, hUbc13 residues (Figure 3D). Furthermore, of the eight residues categorized as strongly affected upon binding of hUbc13, six are within 4 Å of the nearest hUbc13 atom. These chemical shift data are consistent with the crystallographic structures of hMms2-hUbc13 and hUev1a-hUbc13 (*24*, *29*), indicating that the solution structure of hUev1a-hUbc13 is similar to that observed in the crystallographically determined structure.

Interaction with Ubiquitin. Previous titrations of Ub into hUev1a were performed without knowledge of the structure or main chain amide $^1H-^{15}N$ chemical shifts of hUev1a (*28*). Employing the structure of hUev1a determined herein, chemical shift changes for the main chain amide $^1H-^{15}N$ resonances of hUev1a upon binding of Ub indicate that the binding interface is composed of residues from L1, β1, β2, and the C-terminal end of α1 (Figure 1A). The chemical shift data are consistent with our recently determined structure of Ub-bound hMms2 (*26*). Thus, given the similarity in sequence between hMms2 and hUev1a core regions, and the chemical shift data, the superposition of the structure of hUev1a determined herein to the structure of hMms2 bound to Ub (PDB ID 1ZGU) is likely a reasonable model for the hUev1a-Ub interaction (Figure 3B).

Bearing the similarity of the hUev1a-hUbc13 and hMms2-hUbc13 interactions in mind, we have also performed a chemical shift mapping experiment for the ternary complex of acceptor Ub noncovalently bound to the hUbc13-hMms2 complex using conditions where the concentration of acceptor Ub is sufficient to saturate the Ub-hUbc13-hMms2 interaction (Figure 4A). Significant chemical shift changes were observed for Ser^{113} and Asn^{116} of hUbc13 within the loop connecting helices α2 and α3 that is adjacent to the active site cysteine. This loop contributes to the active site cleft on the hUbc13-hMms2 heterodimer, and the chemical shift changes are consistent with an interaction between acceptor Ub and the active site cleft of hUbc13-hMms2. We have also determined chemical shift changes for Ub upon binding hUbc13-hMms2 (Figure 4B). The patterns of observed chemical shift changes are similar to those measured for Ub upon binding hMms2 in the absence of hUbc13 (*26*), with the exceptions that the changes are generally smaller in magnitude, and a significant chemical shift change is not observed for Ub Ser^{65}. Taken together with the hUbc13 chemical shift changes, the chemical shift map for Ub binding to hUbc13-hMms2 can be interpreted as an interaction between the loop on Ub containing Lys^{63} and the active site cleft of hUbc13.

Putative Biological Function of the N-Terminal Tail of hUev1a. The results of our NMR-based chemical shift mapping experiments for the interaction of hUbc13 or Ub with hUev1a indicate that the unstructured N-terminal tail of hUev1a does not interact with Ub or hUbc13. Considering that hUev1a and hMms2 interact with different E3s to achieve their functions, it is possible that the N-terminal tail of hUev1a is involved in recognition of its cognate E3s, TRAF6 or TRAF2, assuming that the TRAF6 RING domain binds hUbc13 in a similar fashion as the interaction between the RING domain from c-Cbl and UbcH7 (*78*). Interestingly, the N-terminal tail of hUev1a is not observed in the crystallographically determined structure of hUev1a-hUbc13 bound to the E3 ligase CHIP (PDB ID 2C2V) (*29*), indicating that it does not interact with CHIP.

Another important aspect regarding the CHIP-hUev1a-hUbc13 structure is that only the U-box domain from CHIP, or the minimal domain required to interact with hUbc13, is observed in the crystal structure (*29*), imposing a serious limitation on functional interpretation, given the general role of E3 ligases in recruiting substrates destined for ubiquitination and cognate E2 enzymes. For example, the structure of the E3-E2 complex c-Cbl−UbcH7 indicates that the RING domain is the principal component from c-Cbl that interacts with UbcH7, with additional interactions involving the N-terminal residues from the TKB domain and linker sequence. Together, the TKB domain, linker sequence, and RING domain form a conserved channel that leads to the active site of UbcH7, and it has been hypothesized that this channel may be involved in interactions with substrate proteins destined for ubiquitination (*78*). However, for the CHIP-hUev1a-hUbc13 complex, there are no structural data regarding interactions between regions proximal to the U-box domain and hUev1a-hUbc13; these regions may be critical for substrate specificity and interact with the N-terminal tail of hUev1a, given that the N-terminus of hUev1a is near to the U-box domain of CHIP. Interestingly, no interactions among these regions are observed in a model for the full CHIP-hUev1a-hUbc13 structure (*29*).

Similarly to the CHIP-hUev1a-hUbc13 interaction, there is a lack of structural data for the TRAF6-hUev1a-hUbc13 complex. The region proximal to the RING domain from TRAF6 contains two TRAF-type zinc-binding domains and differs significantly from the corresponding region in CHIP. As in the case of CHIP, the N-terminal tail of hUev1a can potentially be involved in interactions with the TRAF-type zinc-binding domains, and the nature of this interaction may differ between CHIP and TRAF6.

Implications for PolyUb Chain Formation. On the basis of the similarity of Ub binding between hMms2 and hUev1a, our previous work involving chemical shift mapping of the interaction between Ub and the hMms2-hUbc13 heterodimer (*25*), our structure of the hMms2-Ub complex (*26*), and the recent hUev1a-hUbc13 heterodimer (*29*), it is expected that the role of hUev1a is to bind Ub in such a manner as to position Lys^{63} of the acceptor Ub proximally to the active

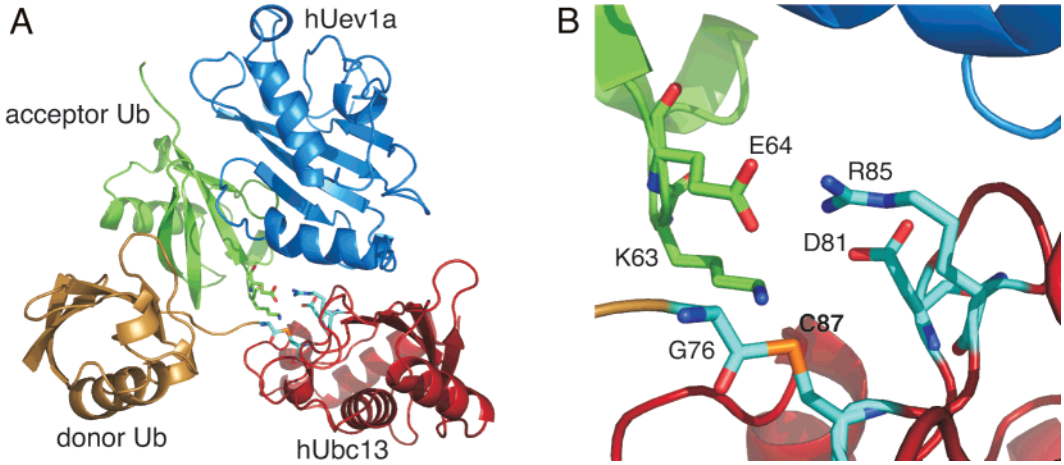

FIGURE 5: Model for the acceptor Ub-hUev1a-hUbc13∼donor Ub tetramer (A). hUev1a is colored in blue, hUbc13 in red, acceptor Ub in green, and donorUb in gold. A close-up view of the active site (B). The side chains from acceptor Ub are colored green, and those from hUbc13 and the C-terminal Gly for donor Ub are colored light blue The ϵ-amino nitrogen of Ub-Lys^{63} is 4.2 Å from the carbonyl carbon of the thioester bond of hUbc13-Cys^{87}.

site cysteine of hUbc13. On the basis of NMR chemical shift mapping experiments presented herein and a recently determined structure for hUev1a-hUbc13 (*29*), it is likely that hUev1a binds Ub and hUbc13 in a similar fashion as hMms2. Therefore, we have used the structure of hUev1a determined in this study, and the structure of hMms2 bound to Ub (*26*), to develop a model for the interaction between acceptor Ub and hUev1a-hUbc13∼Ub (Figure 5) to assess the structural basis of catalysis. The model presented in this study differs from our previous model of the Ub-hMms2−hUbc13∼Ub tetramer (*25*) in two respects that provide new insight into the underlying chemistry. First, the donor ubiquitin was not covalently attached to the active site cysteine of hUbc13. Second, Lys^{63} from the acceptor Ub approached the active site cysteine of hUbc13 from the "outside" of the loop between helices α2 and α3 in hUbc13, whereas our subsequent work, and the chemical shift data presented herein (Figure 4), indicates that it is more likely Lys^{63} approaches the active site of hUbc13 via a cleft on the surface of the hUbc13-hMms2 heterodimer (*26*).

Measurement of reaction rates and ab initio quantum mechanical studies in small thioacetate molecules (*79*−*81*) indicate that there is an important barrier that needs to be overcome for aminolysis of the Ub-hUbc13 thioester bond to occur, to account for observed enzyme-catalyzed rates. It is likely that the acceptor Ub-Lys^{63} ϵ-amino group is deprotonated to promote nucleophilic attack of the carbonyl carbon of the thioester bond. Overcoming this barrier to the reaction may contribute to lowering the activation energy for the reaction.

One of the key structural aspects of our model is that Ub-Lys^{63} is placed in a catalytically competent position by a network of hydrogen bonds involving the side chain carboxyl groups of hUbc13-Asp^{81} and Ub-Glu^{64} (Figure 5). It is generally assumed that deprotonation of acceptor Ub-Lys63 involves the side chain from an Asp/Glu residue acting as a general base. From the model presented herein, two likely candidates for a general base are hUbc13-Asp^{81} and acceptor Ub-Glu^{64}. The importance of Asp^{81} for catalysis has been demonstrated by the fact that Mms2-Ubc13-D81A has impaired catalysis of diUb and Mms2-Ubc13-D81R does not catalyze the synthesis of diUb (*82*).

pK_a calculations are often used to study ionizable side chains in order to gain insight into the catalytic mechanisms of enzymes. However, these methods suffer from a lack of accuracy, partly due to the quality of protein structures employed, and an incomplete understanding of the underlying energetics and dynamics. Regardless of issues surrounding accuracy, some important generalizations have arisen through computational and experimental pK_a studies. For example, Asp^{70} and His^{31} form a semiburied salt bridge in T4 lysozyme, and the measured ΔpK_a for Asp^{70} is ∼−3.5 (*83*). Similarly for *Bacillus circulans* xylanase, Asp^{83} is completely buried and involved in a salt bridge with Arg^{136} and has an experimental ΔpK_a <−2.0 (*84*). Thus, it is reasonable to expect Asp/Glu side chain pK_a values to show negative shifts when they are buried within a protein interior and involved in a salt bridge. For thioredoxin, Asp^{26} is partly buried within a hydrophobic cleft and shows a large increase in pK_a; this increase is also observed in molecular dynamics simulations (*73*).

To probe protein electrostatic interactions in and around the active site when acceptor Ub-Lys^{63} is proximal to the thioester bond, we have performed molecular dynamics simulations with a Ub-hUev1a-hUbc13∼Ub complex, where the distance between the amino nitrogen of Lys^{63} of the donor Ub and the carbonyl carbon of the thioester bond is restrained (see Experimental Procedures). Given that there are no structural data for the Ub-hUev1a-hUbc13∼Ub tetramer, this approach has the advantage of allowing conformational averaging in and around the active site, avoiding the pitfalls associated with using a single model structure. While a fully unrestrained, long time scale molecular dynamics approach would be a more fundamental approach, it is too computationally expensive in the present case, given the size of the system.

ΔpK_a values for hUbc13-Asp^{81}, acceptor Ub-Glu^{64}, and acceptor Ub-Lys^{63} were calculated as previously described (*73*, *85*) for each step of the molecular dynamics simulation. The average ΔpK_a value for acceptor Ub-Lys^{63} over the course of the simulation is ∼0.5. However, when the angle θ (the angle formed between the ϵ-nitrogen of Ub-Lys^{63}, the thioester carbonyl carbon, and the respective carbonyl oxygen) is approximately between 60° and 85° (Figure 6),

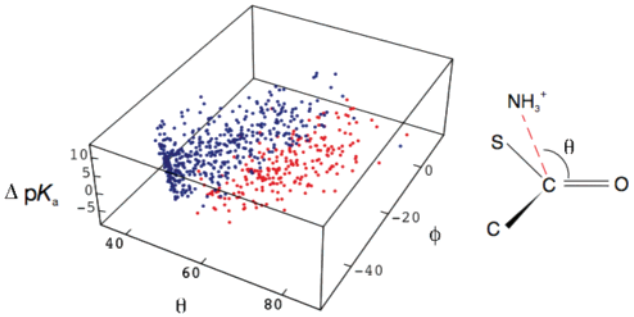

FIGURE 6: Instantaneous ΔpK_a values for acceptor Ub-Lys^{63} calculated from a 200 ps restrained molecular dynamics simulation with a 2 fs time step, with only values greater than 3.5 (blue) and less than −3.5 (red) shown. ϕ indicates the angle between the amino nitrogen of Ub-Lys^{63} and the plane perpendicular to that formed by the four atoms of the thioester carbonyl group.

many of the ΔpK_a values are large and negative, with an average value of −1.8 for $\theta > 70°$. This suggests that as Ub-Lys^{63} approaches the thioester bond at values near the Bürgi−Dunitz angle (107°), deprotonation of the ϵ-amino group and nucleophilic attack on the carbonyl carbon become possible, without the involvement of a general base. Indeed, ΔpK_a values for hUbc13-Asp^{81} and acceptor Ub-Glu^{64} do not show positive shifts during the course of the simulation, indicating that the environment of the active site does not favor protonation of either of these side chains (i.e., they cannot act as a general base). This observation is consistent with their involvement in salt bridge/hydrogen-bonding interactions during the course of the simulation.

The molecular dynamics simulation indicates that the structural and enzymatic role of the hUev1a-hUbc13 heterodimer is to allow for positioning of the acceptor Ub-Lys^{63} through salt bridges with negatively charged side chains such as hUbc13-Asp^{81} and acceptor Ub-Glu^{64}. Ironically, given that deprotonation of Ub-Lys^{63} is likely to be an important catalytic requirement, these salt bridge interactions are expected to upshift the pK_a of Ub-Lys^{63}, a direction opposite to that required for catalysis. However, positioning of the amino group from Ub-Lys^{63} at an angle near the Bürgi−Dunitz angle and proximal to the partially positively charged carbonyl carbon from the thioester bond can give rise to a negative shift for the pK_a of the amino group for Ub-Lys^{63}, consistent with catalytic requirements.

Conclusions. Despite a wealth of structural data for E2 and UEV proteins involved in the catalysis of conjugation of Ub or Ub-like modifiers to target proteins or polyUb chains, the details of the chemical mechanism remain elusive. For example, deprotonation of the target lysine side chain ϵ-amino group by a general base on the E2 enzyme is generally believed to be a key catalytic requirement for the mechanism of isopeptide bond formation. However, a general base has yet to be conclusively identified. Herein, we have determined the structure, main chain dynamics, and interactions for hUev1a using NMR spectroscopy. A structural model for the Ub-hUev1a-hUbc13∼Ub tetramer was developed to gain chemical insight into the catalysis of the synthesis of Lys^{63}-linked diubiquitin chains using restrained molecular dynamics. The key features of the model include maintenance of Ub-Lys^{63} in a catalytically competent conformation through a network of hydrogen bonds involving Ub-Glu^{64} and hUbc13-Asp^{81}. Analysis of the molecular dynamics simulation indicates that if the amino nitrogen of Ub-Lys^{63} approaches the thioester carbonyl carbon near the Bürgi−Dunitz trajectory, a sufficiently large, negative shift in the pK_a of the amino nitrogen could allow deprotonation and nucleophilic attack on the carbonyl carbon, without an Asp or Glu general base being involved.

ACKNOWLEDGMENT

We thank the Canadian National High Field NMR Centre (NANUC) for assistance and use of the facilities. Operation of NANUC is supported by grants from the CIHR, the Natural Sciences and Engineering Research Council of Canada, and the University of Alberta. Electronic structure modeling was performed with the general purpose Linux cluster of AICT (Academic Information and Communication Technologies) at the University of Alberta. We also thank Deryk Webb for spectrometer maintenance, Yanni Batsiolas and Pascal Mercier for computer support, and Lewis E. Kay and Ole W. Sorenson for pulse sequences.

REFERENCES

1. Ben-Neriah, Y. (2002) Regulatory functions of ubiquitination in the immune system, *Nat. Immunol. 3*, 20−26.
2. Chan, N. L., and Hill, C. P. (2001) Defining polyubiquitin chain topology, *Nat. Struct. Biol. 8*, 650−652.
3. Pickart, C. M. (2001) Mechanisms underlying ubiquitination, *Annu. Rev. Biochem. 70*, 503−533.
4. Hershko, A., and Ciechanover, A. (1992) The ubiquitin system for protein degradation, *Annu. Rev. Biochem. 61*, 761−807.
5. Hochstrasser, M. (1996) Ubiquitin-dependent protein degradation, *Annu. Rev. Genet. 30*, 405−439.
6. Jentsch, S. (1992) The ubiquitin-conjugation system, *Annu. Rev. Genet. 26*, 179−207.
7. Hayami, R., Sato, K., Wu, W., Nishikawa, T., Hiroi, J., Ohtani-Kaneko, R., Fukuda, M., and Ohta, T. (2005) Down-regulation of BRCA1-BARD1 ubiquitin ligase by CDK2, *Cancer Res. 65*, 6−10.
8. You, J., and Pickart, C. M. (2001) A HECT domain E3 enzyme assembles novel polyubiquitin chains, *J. Biol. Chem. 276*, 19871−19878.
9. Pickart, C. M. (2000) Ubiquitin in chains, *Trends Biochem. Sci. 25*, 544−548.
10. Pickart, C. M., and Fushman, D. (2004) Polyubiquitin chains: polymeric protein signals, *Curr. Opin. Chem. Biol. 8*, 610−616.
11. Varadan, R., Assfalg, M., Raasi, S., Pickart, C., and Fushman, D. (2005) Structural determinants for selective recognition of a Lys48-linked polyubiquitin chain by a UBA domain, *Mol. Cell 18*, 687−698.
12. Brusky, J., Zhu, Y., and Xiao, W. (2000) UBC13, a DNA-damage-inducible gene, is a member of the error-free postreplication repair pathway in *Saccharomyces cerevisiae*, *Curr. Genet. 37*, 168−174.
13. Hofmann, R. M., and Pickart, C. M. (2001) In vitro assembly and recognition of Lys-63 polyubiquitin chains, *J. Biol. Chem. 276*, 27936−27943.
14. Broomfield, S., Hryciw, T., and Xiao, W. (2001) DNA postreplication repair and mutagenesis in *Saccharomyces cerevisiae*, *Mutat. Res. 486*, 167−184.
15. Finley, D. (2001) Signal transduction. An alternative to destruction, *Nature 412*, 283, 285−286.
16. Hoege, C., Pfander, B., Moldovan, G. L., Pyrowolakis, G., and Jentsch, S. (2002) RAD6-dependent DNA repair is linked to modification of PCNA by ubiquitin and SUMO, *Nature 419*, 135−141.
17. Kanayama, A., Seth, R. B., Sun, L., Ea, C. K., Hong, M., Shaito, A., Chiu, Y. H., Deng, L., and Chen, Z. J. (2004) TAB2 and TAB3 activate the NF-κB pathway through binding to polyubiquitin chains, *Mol. Cell 15*, 535−548.
18. Shi, C. S., and Kehrl, J. H. (2003) Tumor necrosis factor (TNF)-induced germinal center kinase-related (GCKR) and stress-activated protein kinase (SAPK) activation depends upon the E2/

E3 complex Ubc13-Uev1A/TNF receptor-associated factor 2 (TRAF2), *J. Biol. Chem. 278*, 15429−15434.
19. Spence, J., Gali, R. R., Dittmar, G., Sherman, F., Karin, M., and Finley, D. (2000) Cell cycle-regulated modification of the ribosome by a variant multiubiquitin chain, *Cell 102*, 67−76.
20. Andersen, P. L., Zhou, H., Pastushok, L., Moraes, T., McKenna, S., Ziola, B., Ellison, M. J., Dixit, V. M., and Xiao, W. (2005) Distinct regulation of Ubc13 functions by the two ubiquitin-conjugating enzyme variants Mms2 and Uev1A, *J. Cell Biol. 170*, 745−755.
21. Broomfield, S., Chow, B. L., and Xiao, W. (1998) MMS2, encoding a ubiquitin-conjugating-enzyme-like protein, is a member of the yeast error-free postreplication repair pathway, *Proc. Natl. Acad. Sci. U.S.A. 95*, 5678−5683.
22. Deng, L., Wang, C., Spencer, E., Yang, L., Braun, A., You, J., Slaughter, C., Pickart, C., and Chen, Z. J. (2000) Activation of the IκB kinase complex by TRAF6 requires a dimeric ubiquitin-conjugating enzyme complex and a unique polyubiquitin chain, *Cell 103*, 351−361.
23. Zhou, H., Wertz, I., O'Rourke, K., Ultsch, M., Seshagiri, S., Eby, M., Xiao, W., and Dixit, V. M. (2004) Bcl10 activates the NF-κB pathway through ubiquitination of NEMO, *Nature 427*, 167−171.
24. Moraes, T. F., Edwards, R. A., McKenna, S., Pastushok, L., Xiao, W., Glover, J. N., and Ellison, M. J. (2001) Crystal structure of the human ubiquitin conjugating enzyme complex, hMms2-hUbc13, *Nat. Struct. Biol. 8*, 669−673.
25. McKenna, S., Moraes, T., Pastushok, L., Ptak, C., Xiao, W., Spyracopoulos, L., and Ellison, M. J. (2003) An NMR-based model of the ubiquitin-bound human ubiquitin conjugation complex Mms2.Ubc13. The structural basis for lysine 63 chain catalysis, *J. Biol. Chem. 278*, 13151−13158.
26. Lewis, M. J., Saltibus, L. F., Hau, D. D., Xiao, W., and Spyracopoulos, L. (2006) Structural basis for non-covalent interaction between ubiquitin and the ubiquitin conjugating enzyme variant human Mms2, *J. Biomol. NMR 34*, 89−100.
27. Spyracopoulos, L., Lewis, M. J., and Saltibus, L. F. (2005) Main chain and side chain dynamics of the ubiquitin conjugating enzyme variant human Mms2 in the free and ubiquitin-bound states, *Biochemistry 44*, 8770−8781.
28. McKenna, S., Hu, J., Moraes, T., Xiao, W., Ellison, M. J., and Spyracopoulos, L. (2003) Energetics and specificity of interactions within Ub·Uev·Ubc13 human ubiquitin conjugation complexes, *Biochemistry 42*, 7922−7930.
29. Zhang, M., Windheim, M., Roe, S. M., Peggie, M., Cohen, P., Prodromou, C., and Pearl, L. H. (2005) Chaperoned ubiquitylation−crystal structures of the CHIP U box E3 ubiquitin ligase and a CHIP-Ubc13-Uev1a complex, *Mol. Cell 20*, 525−538.
30. McKenna, S., Spyracopoulos, L., Moraes, T., Pastushok, L., Ptak, C., Xiao, W., and Ellison, M. J. (2001) Noncovalent interaction between ubiquitin and the human DNA repair protein Mms2 is required for Ubc13-mediated polyubiquitination, *J. Biol. Chem. 276*, 40120−40126.
31. Sambrook, S., Fritch, E. F., and Maniatis, T. (1989) *Molecular Cloning: A Laboratory Manual*, Cold Spring Harbor Laboratory Press, New York.
32. Zhang, O. W., Kay, L. E., Olivier, J. P., and Forman-Kay, J. D. (1994) Backbone ^{1}H and ^{15}N resonance assignments of the N-terminal SH3 domain of drk in folded and unfolded states using enhanced-sensitivity pulsed-field gradient NMR techniques, *J. Biomol. NMR 4*, 845−858.
33. Delaglio, F., Grzesiek, S., Vuister, G. W., Zhu, G., Pfeifer, J., and Bax, A. (1995) NMRPipe: A multidimensional spectral processing system based on UNIX pipes, *J. Biomol. NMR 6*, 277−293.
34. Johnson, B. A., and Blevins, R. A. (1994) NMR View: A computer program for the visualization and analysis of NMR data, *J. Biomol. NMR 4*, 603−614.
35. Muhandiram, D. R., and Kay, L. E. (1994) Gradient-enhanced triple-resonance three-dimensional NMR experiments with improved sensitivity, *J. Magn. Reson., Ser. B 103*, 203−216.
36. Wittekind, M., and Mueller, L. (1993) HNCACB, a high-sensitivity 3D NMR experiment to correlate amide-proton and nitrogen resonances with the alpha- and beta-carbon resonances in proteins, *J. Magn. Reson., Ser. B 101*, 201−205.
37. Grzesiek, S., and Bax, A. (1992) Correlating backbone amide and side-chain resonances in larger proteins by multiple relayed triple resonance NMR, *J. Am. Chem. Soc. 114*, 6291−6293.
38. Ikura, M., Kay, L. E., and Bax, A. (1990) A novel approach for sequential assignment of ^{1}H, ^{13}C, and ^{15}N spectra of larger proteins: Heteronuclear triple-resonance three-dimensional NMR spectroscopy. Application to calmodulin, *Biochemistry 29*, 4659−4667.
39. Grzesiek, S., Anglister, J., and Bax, A. (1993) Correlation of backbone amide and aliphatic side-chain resonances in ^{13}C/^{15}N-enriched proteins by isotropic mixing of ^{13}C magnetization, *J. Magn. Reson., Ser. B 101*, 114−119.
40. Montelione, G. T., Lyons, B. A., Emerson, S. D., and Tashiro, M. (1992) An efficient triple resonance experiment using carbon-13 isotropic mixing for determining sequence-specific resonance assignments of isotopically enriched proteins, *J. Am. Chem. Soc. 114*, 10974−10975.
41. Bax, A., Clore, G. M., and Gronenborn, A. M. (1990) ^{1}H-^{1}H correlation via isotropic mixing of ^{13}C magnetization, a new three-dimensional approach for assigning ^{1}H and ^{13}C spectra of ^{13}C-enriched proteins, *J. Magn. Reson. 88*, 425−431.
42. Kay, L. E., Xu, G. Y., Singer, A. U., Muhandiram, D. R., and Forman-Kay, J. D. (1993) A gradient-enhanced HCCH-TOCSY experiment for recording side-chain ^{1}H and ^{13}C correlations in H_2O samples of proteins, *J. Magn. Reson., Ser. B 101*, 333−337.
43. Yang, D. W., Zheng, Y., Liu, D. J., and Wyss, D. F. (2004) Sequence-specific assignments of methyl groups in high-molecular weight proteins, *J. Am. Chem. Soc. 126*, 3710−3711.
44. Vuister, G. W., and Bax, A. (1993) Quantitative *J* correlation: a new approach for measuring homonuclear three-bond $J(H^{N}H^{\alpha})$ coupling-constants in ^{15}N-enriched proteins, *J. Am. Chem. Soc. 115*, 7772−7777.
45. Archer, S. J., Ikura, M., Torchia, D. A., and Bax, A. (1991) An alternative 3D NMR technique for correlating backbone ^{15}N with side chain Hβ resonances in larger proteins, *J. Magn. Reson. 95*, 636−641.
46. Yamazaki, T., Forman-Kay, J. D., and Kay, L. E. (1993) Two-dimensional NMR experiments for correlating ^{13}Cβ and ^{1}Hδ/ϵ chemical shifts of aromatic residues in ^{13}C-labeled proteins via scalar couplings, *J. Am. Chem. Soc. 115*, 11054−11055.
47. Meissner, A., and Sorensen, O. W. (1999) Optimization of three-dimensional TROSY-type HCCH NMR correlation of aromatic ^{1}H-^{13}C groups in proteins, *J. Magn. Reson. 139*, 447−450.
48. Meissner, A., and Sorensen, O. W. (2000) Suppression of diagonal peaks in three-dimensional protein NMR TROSY-type HCCH correlation experiments, *J. Magn. Reson. 144*, 171−174.
49. Pervushin, K., Riek, R., Wider, G., and Wuthrich, K. (1998) Transverse relaxation-optimized spectroscopy (TROSY) for NMR studies of aromatic spin systems in ^{13}C-labeled proteins, *J. Am. Chem. Soc. 120*, 6394−6400.
50. Neri, D., Szyperski, T., Otting, G., Senn, H., and Wuthrich, K. (1989) Stereospecific nuclear magnetic resonance assignments of the methyl groups of valine and leucine in the DNA-binding domain of the 434 repressor by biosynthetically directed fractional ^{13}C labeling, *Biochemistry 28*, 7510−7516.
51. Goddard, T. D., and Kneller, D. G., SPARKY 3, University of California, San Francisco.
52. Gagné, S. M., Li, M. X., and Sykes, B. D. (1997) Mechanism of direct coupling between binding and induced structural change in regulatory calcium binding proteins, *Biochemistry 36*, 4386−4392.
53. Cornilescu, G., Delaglio, F., and Bax, A. (1999) Protein backbone angle restraints from searching a database for chemical shift and sequence homology, *J. Biomol. NMR 13*, 289−302.
54. Gagné, S. M., Tsuda, S., Li, M. X., Chandra, M., Smillie, L. B., and Sykes, B. D. (1994) Quantification of the calcium-induced secondary structure changes in the regulatory domain of troponin-C, *Protein Sci. 3*, 1961−1974.
55. Hwang, T. L., van Zijl, P. C. M., and Mori, S. (1998) Accurate quantitation of water-amide proton exchange rates using the phase-modulated CLEAN chemical EXchange (CLEANEX-PM) approach with a fast-HSQC (FHSQC) detection scheme, *J. Biomol. NMR 11*, 221−226.
56. Willard, L., Ranjan, A., Zhang, H. Y., Monzavi, H., Boyko, R. F., Sykes, B. D., and Wishart, D. S. (2003) VADAR: a web server for quantitative evaluation of protein structure quality, *Nucleic Acids Res. 31*, 3316−3319.
57. Brunger, A. T., Adams, P. D., Clore, G. M., DeLano, W. L., Gros, P., Grosse-Kunstleve, R. W., Jiang, J. S., Kuszewski, J., Nilges, M., Pannu, N. S., Read, R. J., Rice, L. M., Simonson, T., and Warren, G. L. (1998) Crystallography & NMR system: A new

software suite for macromolecular structure determination, *Acta Crystallogr. D 54*, 905−921.
58. Laskowski, R. A., Rullmann, J. A., MacArthur, M. W., Kaptein, R., and Thornton, J. M. (1996) AQUA and PROCHECK-NMR: programs for checking the quality of protein structures solved by NMR, *J. Biomol. NMR 8*, 477−486.
59. DeLano, W. L. (2002).
60. Koradi, R., Billeter, M., and Wüthrich, K. (1996) MOLMOL: a program for display and analysis of macromolecular structures, *J. Mol. Graphics 14*, 51−55, 29−32.
61. Wolfram, S. (1996) *The Mathematica Book*, 3rd ed., Wolfram Media/Cambridge University Press, New York.
62. Dominguez, C., Boelens, R., and Bonvin, A. M. (2003) HADDOCK: a protein−protein docking approach based on biochemical or biophysical information, *J. Am. Chem. Soc. 125*, 1731−1737.
63. Frisch, M. J., Trucks, G. W., Schlegel, H. B., Scuseria, G. E., Robb, M. A., Cheeseman, J. R., Montgomery, Jr., J. A., Vreven, T., Kudin, K. N., Burant, J. C., Millam, J. M., Iyengar, S. S., Tomasi, J., Barone, V., Mennucci, B., Cossi, M., Scalmani, G., Rega, N., Petersson, G. A., Nakatsuji, H., Hada, M., Ehara, M., Toyota, K., Fukuda, R., Hasegawa, J., Ishida, M., Nakajima, T., Honda, Y., Kitao, O., Nakai, H., Klene, M., Li, X., Knox, J. E., Hratchian, H. P., Cross, J. B., Bakken, V., Adamo, C., Jaramillo, J., Gomperts, R., Stratmann, R. E., Yazyev, O., Austin, A. J., Cammi, R., Pomelli, C., Ochterski, J. W., Ayala, P. Y., Morokuma, K., Voth, G. A., Salvador, P., Dannenberg, J. J., Zakrzewski, V. G., Dapprich, S., Daniels, A. D., Strain, M. C., Farkas, O., Malick, D. K., Rabuck, A. D., Raghavachari, K., Foresman, J. B., Ortiz, J. V., Cui, Q., Baboul, A. G., Clifford, S., Cioslowski, J., Stefanov, B. B., Liu, G., Liashenko, A., Piskorz, P., Komaromi, I., Martin, R. L., Fox, D. J., Keith, T., Al-Laham, M. A., Peng, C. Y., Nanayakkara, A., Challacombe, M., Gill, P. M. W., Johnson, B., Chen, W., Wong, M. W., Gonzalez, C., and Pople, J. A. (2004) Gaussian 03, Revision C.02, Gaussian, Inc., Wallingford, CT.
64. Foresman, J. B., and Frish, A. (1996) *Exploring Chemistry with Electronic Structure Methods*, 2nd ed., Gaussian, Inc., Pittsburgh, PA.
65. Bayly, C. I., Cieplak, P., Cornell, W. D., and Kollman, P. A. (1993) A well-behaved electrostatic potential based method using charge restraints for deriving atomic charges−the RESP model, *J. Phys. Chem. 97*, 10269−10280.
66. Cieplak, P., Cornell, W. D., Bayly, C., and Kollman, P. A. (1995) Application of the multimolecule and multiconformational RESP methodology to biopolymers−charge derivation for DNA, RNA, and proteins, *J. Comput. Chem. 16*, 1357−1377.
67. Case, D. A., Cheatham, T. E., Darden, T., Gohlke, H., Luo, R., Merz, K. M., Onufriev, A., Simmerling, C., Wang, B., and Woods, R. J. (2005) The Amber biomolecular simulation programs, *J. Comput. Chem. 26*, 1668−1688.
68. Cornell, W. D., Cieplak, P., Bayly, C. I., Gould, I. R., Merz, K. M., Ferguson, D. M., Spellmeyer, D. C., Fox, T., Caldwell, J. W., and Kollman, P. A. (1995) A 2nd generation force field for the simulation of proteins, nucleic acids, and organic molecules, *J. Am. Chem. Soc. 117*, 5179−5197.
69. Wang, J. M., Cieplak, P., and Kollman, P. A. (2000) How well does a restrained electrostatic potential (RESP) model perform in calculating conformational energies of organic and biological molecules?, *J. Comput. Chem. 21*, 1049−1074.
70. Ryckaert, J. P., Ciccotti, G., and Berendsen, H. J. C. (1977) Numerical integration of Cartesian equations of motion of a system with constraints−molecular-dynamics of *n*-alkanes, *J. Comput. Phys. 23*, 327−341.
71. Berendsen, H. J. C., Postma, J. P. M., van Gunsteren, W. F., Dinola, A., and Haak, J. R. (1984) Molecular dynamics with coupling to an external bath, *J. Chem. Phys. 81*, 3684−3690.
72. Onufriev, A., Bashford, D., and Case, D. A. (2004) Exploring protein native states and large-scale conformational changes with a modified generalized Born model, *Proteins 55*, 383−394.
73. Simonson, T., Carlsson, J., and Case, D. A. (2004) Proton binding to proteins: pK_a calculations with explicit and implicit solvent models, *J. Am. Chem. Soc. 126*, 4167−4180.
74. Homans, S. W. (2005) Probing the binding entropy of ligand-protein interactions by NMR, *ChemBioChem 6*, 1585−1591.
75. Spyracopoulos, L. (2005) Thermodynamic interpretation of protein dynamics from NMR relaxation measurements, *Protein Pept. Lett. 12*, 235−240.
76. Zhang, F., and Brüschweiler, R. (2002) Contact model for the prediction of NMR N−H order parameters in globular proteins, *J. Am. Chem. Soc. 124*, 12654−12655.
77. Yang, D. W., and Kay, L. E. (1996) Contributions to conformational entropy arising from bond vector fluctuations measured from NMR-derived order parameters: Application to protein folding, *J. Mol. Biol. 263*, 369−382.
78. Zheng, N., Wang, P., Jeffrey, P. D., and Pavletich, N. P. (2000) Structure of a c-Cbl-UbcH7 complex: RING domain function in ubiquitin-protein ligases, *Cell 102*, 533−539.
79. Conners, K. A., and Bender, M. L. (1961) The kinetics of alkaline hydrolysis and *n*-butylaminolysis of ethyl *p*-nitrobenzoate and ethyl *p*-nitrothiolbenzoate, *J. Org. Chem. 26*, 2498−2504.
80. Yang, W., and Drueckhammer, D. G. (2000) Computational studies of the aminolysis of oxoesters and thioesters in aqueous solution, *Org. Lett. 2*, 4133−4136.
81. Yang, W., and Drueckhammer, D. G. (2001) Understanding the relative acyl-transfer reactivity of oxoesters and thioesters: Computational analysis of transition state delocalization effects, *J. Am. Chem. Soc. 123*, 11004−11009.
82. VanDemark, A. P., Hofmann, R. M., Tsui, C., Pickart, C. M., and Wolberger, C. (2001) Molecular insights into polyubiquitin chain assembly: crystal structure of the Mms2/Ubc13 heterodimer, *Cell 105*, 711−720.
83. Dong, F., and Zhou, H. X. (2002) Electrostatic contributions to T4 lysozyme stability: solvent-exposed charges versus semi-buried salt bridges, *Biophys J 83*, 1341−1347.
84. Joshi, M. D., Hedberg, A., and McIntosh, L. P. (1997) Complete measurement of the pK_a values of the carboxyl and imidazole groups in *Bacillus circulans* xylanase, *Protein Sci. 6*, 2667−2670.
85. Mongan, J., Case, D. A., and McCammon, J. A. (2004) Constant pH molecular dynamics in generalized Born implicit solvent, *J. Comput. Chem. 25*, 2038−2048.

BI060631R